Promotion effect of ZnO on the photocatalytic activity of coupled Al_2O_3-Nd_2O_3-ZnO composites prepared by the sol – gel method in the degradation of phenol

J.E. Casillas [a], F. Tzompantzi [b,*], S.G. Castellanos [a], G. Mendoza-Damián [b], R. Pérez-Hernández [c], A. López-Gaona [b], A. Barrera [a,*]

[a] Laboratorio de Nanomateriales Catalíticos, Centro Universitario de la Ciénega, Universidad de Guadalajara, Av. Universidad, No. 1115, Col. Linda Vista, C.P. 47820, Ocotlán Jal., México
[b] Depto. de Química, Área de Catálisis, Universidad Autónoma Metropolitana – Iztapalapa, Av. San Rafael Atlixco 189, C.P. 09340, Cd. de México, México
[c] Laboratorio de Nanocatálisis, Depto. de Tecnología de Materiales, Instituto Nacional de Investigaciones Nucleares, Carr. México-Toluca S/N, La Marquesa, Ocoyoacac, Edo. De México, C.P. 52750, México

ARTICLE INFO

ABSTRACT

The photocatalytic activity of coupled Al_2O_3-Nd_2O_3-ZnO composites (Al-Nd-Zn-x; where x = 0.8, 1.2, 2.0, 5.0, and 15.0 wt% of ZnO) prepared by the sol-gel method was studied in the photo-degradation of phenol in aqueous medium. The Al-Nd-Zn-x composites were characterized by physical adsorption of N_2, XRD, TEM, SEM, Raman, UV–vis, XPS and fluorescence spectroscopies. Al-Nd-Zn-x composites with ZnO concentration in the range 0.8–2.0 wt% showed high efficiency to photo-convert phenol and mineralize dissolved organic carbon to CO_2 with UV light irradiation. The Al-Nd-Zn-1.2 composite was the material with the highest efficacy to photodegradate phenol in aqueous medium photo-converting about 90.0% of phenol and mineralizing 75.0% of dissolved organic carbon after 3 h of UV light. It is proposed that the intimate contact between Al_2O_3, Nd_2O_3 and ZnO phases of the coupled Al-Nd-Zn-x composites are beneficial characteristics for the separation of the photogenerated charge carriers in order to decrease the recombination rate of photogenerated electron-hole pairs. These Al-Nd-Zn-x composites are characterized by a high BET specific surface area and a bimodal pore size distribution which are excellent characteristics for the adsorption and diffusion of phenol molecules to the active sites resulting in enhanced photocatalytic properties for the degradation of phenol in aqueous medium.

© 2017 Published by Elsevier B.V.

1. Introduction

Environmental pollution caused by hazardous substances from wastewater of industrial processes is a worldwide problem. As an example, the emission of phenolic compounds to the environment is among the most critical. The source of phenolic compounds includes the wastewater of many industrial process such as petroleum refining, plastic and resin production, paper processing, carbon liquefaction and pharmaceutical industry among others [1,2]. Among these contaminants phenol is a highly toxic organic compound and plays a main role due to their extensive use. Phenol is used commonly as pesticide in agriculture from which it is filtered within the soils and later transported by the raining water contaminating the rivers, lakes and drinkable water

sources [3,4]. The elimination of such recalcitrant organic contaminant from the waste water is a great problem and whose solution is urgent and not easy [5,6]. The phenolic compounds and their derivative that are released to the environment are very stable and persistent for which it has no capability of assimilation requiring a very long time for its natural degradation, therefore is necessary the application of efficient methods for its rapid degradation [7]. Concerning to it, considerable efforts has been addressed to develop methods for eliminating highly toxic organic contaminants such as phenol from the wastewaters. It has been tried to carry out the treatment of these contaminant by physicochemical and/or biological methods; however, these treatments usually are little effective due to that these organic compounds have high chemical stability and low biodegradability [5,8]. In order to abate the impact caused by the wastewater of the industrial effluents, advanced oxidation processes (AOP) have been implemented in the last years as a technological feasible alternative for the treatment of the industrial effluents. The AOP consist basically in the formation of highly oxidant hydroxyl radicals which contribute to the

total destruction of the contaminant organic molecules and mineralization of dissolved carbon to CO_2. The photocatalytic method is among the more used AOP and consists in the aceleration of a photoreaction by mean of a photocatalyst prepared on the base of a semiconductor material and UV or visible light as irradiation source [5,9]. TiO_2 is the most studied semiconductor material for eliminating organic contaminants [10–13]. Materials other than TiO_2 have been recently reported as semiconductors for photocatalytic applications, among them, Bi_2WO_6 nano-composites modified with reduced graphene oxide [14], layered double hydroxides [15–18], and Cr, Mn, Fe, Ni, Cu as substituting metals in $CeVO_4$ [19]. Alternatively, we have reported recently the use of noble metal oxides such as PdO supported on alumina modified with neodymium oxide as interesting photocatalysts for the degradation of contaminant organic compounds such as 2, 4-D and phenol in aqueous medium [20,21]. Furthermore, it has been demonstrated recently that γ-Al_2O_3 exhibit relatively high photocatalytic activity in the degradation of organic compounds in aqueous medium after 6 h of UV irradiation [22]. However, it is still necessary to improve the photocatalytic systems based on γ-Al_2O_3 because they show high reaction times to reach the maximum photoconversion of organic molecules in aqueous medium. One way in order to improve the photocatalytic activity of γ-Al_2O_3 is by addition of rare earth oxides such as Nd_2O_3 and by coupling with semiconductor oxides such as ZnO. In this sense, the study of the photo-catalytic performance of materials based on Al_2O_3-Nd_2O_3 coupled with ZnO could be a very attractive proposal in order to find out new photo-catalytic materials with high activity and lower cost. It is well known that g-Al_2O_3 is a cheap material, and is widely used as a support for catalysts in many catalytic processes because of its high specific surface area and excellent thermal stability. However, alumina shows insulating properties due to its high "band gap" energy ($E_g > 5$ eV) [23]. In spite of that alumina has insulating properties however it has been shown the feasibility of using Al_2O_3 synthesized by the sol-gel method as a catalyst for the photo-mineralization of hazardous organic molecules [22]. On the other hand, it is also known that Nd_2O_3 is the third more abundant element among lanthanides and can also be used as a stabilizer of the γ-Al_2O_3 surface area [24,25] as well as a doping agent for the TiO_2 semiconductor for photo-catalytic purposes [26–31]. On the other hand, the beneficial effects of use ZnO as doping agent of TiO_2 has been reported in waste water treatment [14,32–34]. Regarding to it, it is known that ZnO is an n-type semiconductor with a band gap energy of 3.2 eV [35]. Furthermore, many reports on ZnO nanostructures combined with other semiconductors have shown recently enhanced light absorption and improved charge carrier transfer [36,37]. With this in mind, it seems to be very interesting to investigate the effect of promotion of ZnO on the photo-catalytic performance of coupled Al_2O_3-Nd_2O_3-ZnO composites in the photodegradation of organic compounds in aqueous medium. In the present work, we have investigated the photo-catalytic performance of coupled Al_2O_3-Nd_2O_3-ZnO composites prepared by the sol-gel method in the photodegradation of phenol in aqueous medium. The physicochemical properties of coupled Al_2O_3-Nd_2O_3-ZnO composites were studied by N_2 physisorption, X-ray diffraction, transmission electron microscopy, scanning electron microscopy and Raman, UV–vis and XP spectroscopies.

2. Materials and methods

2.1. Synthesis of Al_2O_3-Nd_2O_3-ZnO composites

Al_2O_3-Nd_2O_3-ZnO composite oxides (Al-Nd-Zn-*x*, where *x* = 0.8, 1.2, 2.0, 5.0 and 15.0 wt% of ZnO) were prepared by the sol-gel method. The concentration of 15 wt% of Nd_2O_3 was kept constant

in all the composite oxides. Briefly the method of preparation of Al-Nd-Zn-*x* composite oxides is described as follows: a required volume of aluminum tri-sec-butoxide (Aldrich) was dissolved in a three mouth glass flask containing 10 mL of 2-methylpentane 2, 4-diol (Aldrich). The alumina precursor solution was heated at 70 °C under continuous stirring for 1 h. After that, the required amounts of neodymium acetylacetonate (Aldrich) and zinc acetylacetonate (Aldrich) previously dissolved in toluene (Aldrich) at 40 °C were added to the alumina precursor solution. The Al-Nd-Zn-*x* precursor solution was heated at 70 °C for 1 h with continuous stirring. Then, a volume of 10 mL of deionised water was added to the solution drop wise to carry out the hydrolysis of the Al-Nd-Zn-*x* precursor solution. The obtained gels were aged at 90 °C for 3 h and then dried at 120 °C for 12 h followed by calcination under static air at 550 °C for 4 h at a heating rate of 10 °C min^{-1} to obtain Al_2O_3-Nd_2O_3-ZnO composite oxides. Pure γ-Al_2O_3 was prepared following the sol-gel preparation method described above but without the addition of neodymium acetylacetonate and zinc acetylacetonate. Pure Nd_2O_3 and ZnO were prepared by thermal decomposition of neodymium acetylacetonate and zinc acetylactonate powder at 800 °C for 5 h and 600 °C for 3 h respectively.

2.2. Characterization of Al_2O_3-Nd_2O_3-ZnO composites

The structural characteristics of Al-Nd-Zn-*x* composite oxides were determined by X-ray diffraction by using a Theta-Theta model X-ray diffractometer (from STOE). X-ray diffraction patterns were recorded at room temperature in the 2θ angle range between 5° and 80°, with a 2q step of 0.02° and 5 s per step, using a Cu Ka (l = 0.154 nm) electromagnetic radiation source. Identification of the diffraction peaks from the XRD patterns was carried out using the JCPDS database included in the software of the equipment. The structural characteristics of Al-Nd-Zn-*x* composite oxides were also studied by Raman spectroscopy using a Raman DXR Thermo Scientific Microscope. Raman spectra were recorded in the 100–3500 cm^{-1} wavenumber range. The excitation line of the Nd:YVO4DPSS laser source was 532 nm with a laser power of 10 mW. TEM images of the Al-Nd-Zn-*x* composite oxides were obtained using a transmission electron microscope, HRTEM Jeol 2100F, with a power of 200 kV and a resolution of 0.186 nm. SEM images of Al-Nd-Zn-*x* composite oxides were obtained using a scanning electron microscope, HRSEM Jeol 7600F, with a power of 30 kV and a resolution of 1 nm. The textural properties of Al-Nd-Zn-*x* composite oxides were studied by physical adsorption of nitrogen at its saturation temperature (−196.5 °C) by using an Autosorb system (IQ model from Quantachrome). Samples were outgassed with He flow at 300 °C for 5 h previous to the measurements. Specific surface area was calculated by using the Brunauer-Emmet-Teller (BET) equation. Pore size distributions were calculated from desorption branch of nitrogen isotherms by applying the Barrett, Joyner and Halenda (BJH) method. The optical properties of γ-Al-Nd-Zn-*x* composite oxides were studied by UV–vis diffuse reflectance spectroscopy using an UV–vis CARY 300 SCAN spectrophotometer in the wavelength range of 190–800 nm with a scan speed of 600 nm min^{-1}; intervals of data collection of 1 nm and a change of the light source at a wavelength of 350 nm. Band gap energy (E_g) values of γ-Al_2O_3, Nd_2O_3, ZnO and Al-Nd-Zn-*x* composite oxides were determined by using the Kubelka-Munk function and the relation between the absorption edge and the absorbance according to the Eq. (1) [38,39]:

$$\alpha h v = B(h v - E_g)^2 \qquad (1)$$

Where α is the absorbance, hv is the photon energy, E_g is the band gap energy and B is a feature constant for the materials. The band gap energies values were determined by plotting the square root of the Kubelka-Munk function multiplied by the photon energy versus

the photon energy and extrapolating the linear part of the curve to zero, it is by plotting $(\alpha h\nu)^{1/2}$ versus $h\nu$, relation known as graph of Tauc [40]. Surface properties of Al-Nd-Zn-*x* ternary oxides were studied by X-ray photoelectron spectroscopy (XPS). The XP spectra were recorded on a VG ESCALAB 250 apparatus after excitation with a monochromatic Al Kα radiation ($h\nu$= 1486.6 eV). Samples were embedded onto Indium foils which were pressed manually and placed to a holder. Calibration of the energy position of an XPS peak was performed by using the binding energy of carbon 1 s peak at 284.8 eV. The unresolved XP spectra for the Nd 3d, Al 2p and Zn transition were fitted by using a standard Gaussian function. The binding energies values were assigned to the corresponding oxidation state according to literature data. Fluorescence experiments of Al-Nd-Zn-*x* composite oxides were carried out using a Fluorescence Varian Caryeclipse spectrophotometer using a excitation wavelength of 250 nm.

2.3. Photocatalytic degradation of phenol

The phenol photo-catalytic degradation was carried out using a 1 L batch-type round bottom cylindrical glass photo-reactor surrounded by a double-wall glass jacket. Previous to photo-degradation experiments, an aqueous solution of phenol (99.9%, Sigma-Aldrich) with a concentration of 80 ppm/L was bubbled with air during 2 h. After that, 200 mL of the phenol dissolution was put into the glass photo-reactor followed by the addition of 200 mg of the Al-Nd-Zn-*x* photocatalyst to give a concentration of 1 mg of photo-catalyst/mL of phenol solution. Under continuous aeration (1 mL/s) and stirring, the phenol dissolution was irradiated using a protected quartz tube with a Pen-Ray UV power supply lamp (UVP products) of a typical wavelength of 254 nm and intensity of 4400 mWcm^{-2}, immersed into the solution. Prior to the photo-catalytic experiments, the phenol solution and the catalyst were kept in contact for 1 h without irradiation in order to determine the adsorption capacity of the solids. Then, the UV lamp was turned on. To follow the photo-degradation of phenol as a function of time, samples of the irradiated solution were taken each every hour from the photo-reactor using a filter for a period of 6 h. The phenol degradation was followed by UV–vis spectroscopy, employing a CARY 100 spectrophotometer measuring the absorbance at λ = 270 nm and using the Lambert and Beer equation for the calculation of the concentration of photo-converted phenol. The relative concentration (C/Co) data of photo-converted phenol were adjusted to a pseudo first order kinetics of Langmuir-Hinshelwood model type. The total organic carbon (TOC) was followed using a TOC-V$_{CEN}$ Shimadzu 5000 analyzer (catalytic oxidation on Pt at 680 °C). Calibration runs were performed injecting known amounts of potassium phthalate.

3. Results and discussion

3.1. Porous texture of Al$_2$O$_3$-Nd$_2$O$_3$-ZnO composite oxides

The nitrogen adsorption – desorption isotherms of Al$_2$O$_3$, Nd$_2$O$_3$, ZnO, Al-Nd and Al-Nd-Zn-*x* composite oxides prepared by the sol-gel method are shown in Fig. S1 (left). The isotherms of Al$_2$O$_3$, Al-Nd and Al-Nd-Zn-*x* are of type IV according to the classification of the IUPAC which are typical of mesoporous materials [41,42]. Whereas, the isotherms of Nd$_2$O$_3$ and ZnO are characteristic of non-porous materials. The isotherm of Al$_2$O$_3$ shows a hysteresis loop of the type H1 being associated with mesoporous materials containing well-defined cylindrical-like pore channels [41,42]. The isotherm of Al$_2$O$_3$ is modified with addition of Nd$_2$O$_3$ and ZnO due to the presence of different pore sizes in the materials. This is corroborated from their pore size distributions (PSD) (Fig. S1,

Table 1
Textural properties of γ-Al$_2$O$_3$, Al-Nd and Al-Nd-Zn-*x* ternary oxides prepared by the sol-gel method. For comparison, textural properties of Nd$_2$O$_3$, ZnO and Al$_2$O$_3$ Catapal B are also shown.

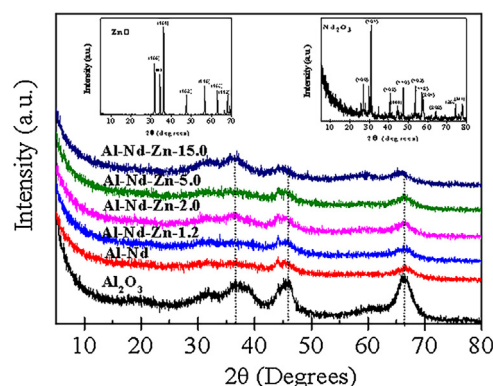| Photocatalyst	S$_{BET}$ (m^2 g^{-1})	V$_{MICRO}$ (cm^3 g^{-1})	V$_{MESO}$ (cm^3 g^{-1})	APD (nm)
γ-Al$_2$O$_3$-SG	232.0	0.26	1.00	16.2
Al-Nd	243.0	0.26	0.59	9.7
Al-Nd-Zn-0.8	250.0	0.26	0.53	8.4
Al-Nd-Zn-1.2	272.0	0.30	0.70	10.3
Al-Nd-Zn-2.0	267.0	0.27	0.52	8.0
Al-Nd-Zn-5.0	256.0	0.27	0.60	9.4
Al-Nd-Zn-15.0	137.0	0.14	0.30	8.3
Nd$_2$O$_3$	6.0	0.01	0.03	–
ZnO	6.0	0.01	0.08	–
Al$_2$O$_3$ Catapal B	213.0	0.17	0.28	5.4

Fig. 1. XRD patterns of γ-Al$_2$O$_3$ and Al-Nd-Zn-*x* composites prepared by the sol gel method. Inset: XRD patterns of pristine Nd$_2$O$_3$ and ZnO.

right). There is a shifting in the modal peak of the PSD of the composite oxides from a pore size of 12 nm for the γ-Al$_2$O$_3$ to smaller pore sizes with the addition of Nd$_2$O$_3$ and ZnO. Al$_2$O$_3$ exhibits a symmetrical PSD in the pore size range of 4–30 nm indicating the presence of uniform pore sizes. Al-Nd and Al-Nd-Zn-0.8 composite oxide exhibit a bimodal pore size distribution with modal peaks at 8.0 nm and 5.0 nm. However, an intense modal peak at about 5.7 nm with asymmetry toward large pore sizes is observed in the PSD of Al-Nd-Zn-*x* with 1.2 and 2.0 wt% of ZnO. On the other hand, the S$_{BET}$ of Al$_2$O$_3$, Nd$_2$O$_3$, ZnO, Al-Nd, and Al-Nd-Zn-*x* composite oxides is shown in Table 1. Pure Al$_2$O$_3$ shows a S$_{BET}$ of 232.0 m^{2}g^{-1} that is improved about 5.0% in the Al-Nd composite (S$_{BET}$ = 243.0 m^{2}g^{-1}). In addition, S$_{BET}$ of Al-Nd is improved about 12.0% by doping with ZnO reaching a maximum value (272.0 m^{2}g^{-1}) in the Al-Nd-Zn-1.2 composite oxide. This observation suggests that Nd$_2$O$_3$ and ZnO act as textural promoters of Al$_2$O$_3$. For ZnO concentration higher than 5.0%, S$_{BET}$ of Al-Nd-Zn-*x* decreased significantly and Al-Nd-Zn-15.0 showed a S$_{BET}$ of 137.0 m^{2}g^{-1}. The specific meso-pore volume (V$_{MESO}$) and average pore diameter (APD) of Al$_2$O$_3$ were the highest values (1.0 cm^{3}g^{-1} and 16.2 nm respectively) in the material series and decreased with addition of Nd$_2$O$_3$ and ZnO although Al-Nd-Zn-1.2 exhibited a high V$_{MESO}$ (0.70 cm^{3}g^{-1}) due to the broadening of its pore structure (Table 1). On the other hand, with the exception of Al-Nd-Zn-15.0 showing a low specific micro-pore volume (V$_{MICRO}$ = 0.14 cm^{3}g^{-1}), Al-Nd-Zn-*x* composite oxides showed a V$_{MICRO}$ approximately constant (~0.27 cm^{3}g^{-1}).

3.2. Structure properties of Al$_2$O$_3$-Nd$_2$O$_3$-ZnO ternary oxides

Fig. 1 shows the XRD patterns of Al$_2$O$_3$, Al-Nd and Al-Nd-Zn-*x* composite oxides. XRD pattern of bare Al$_2$O$_3$ shows diffraction peaks at 36.9, 46.1 and 66.6° corresponding to the γ-Al$_2$O$_3$ phase
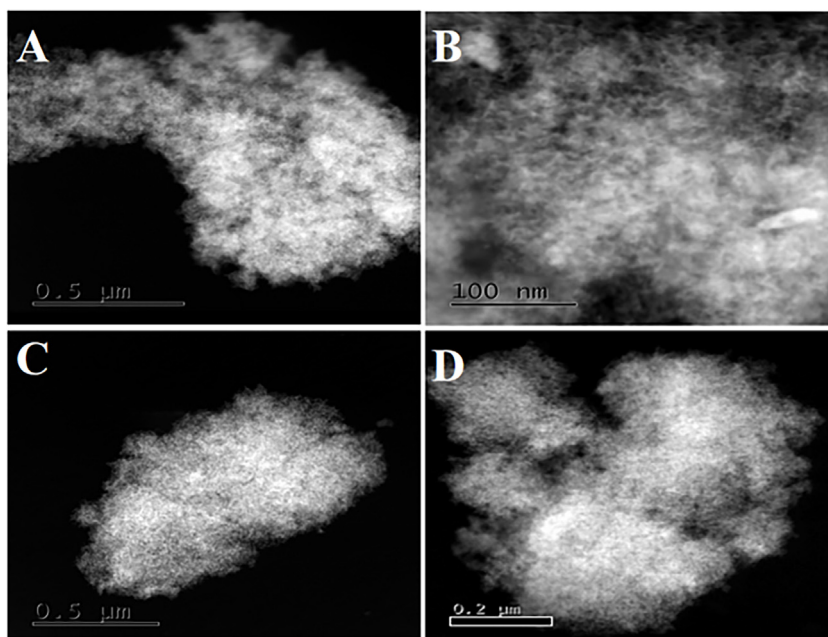
Fig. 2. TEM images of Al-Nd-Zn-1.2 (A, B) and Al-Nd-Zn-2 (C, D) composites prepared by the sol-gel method.
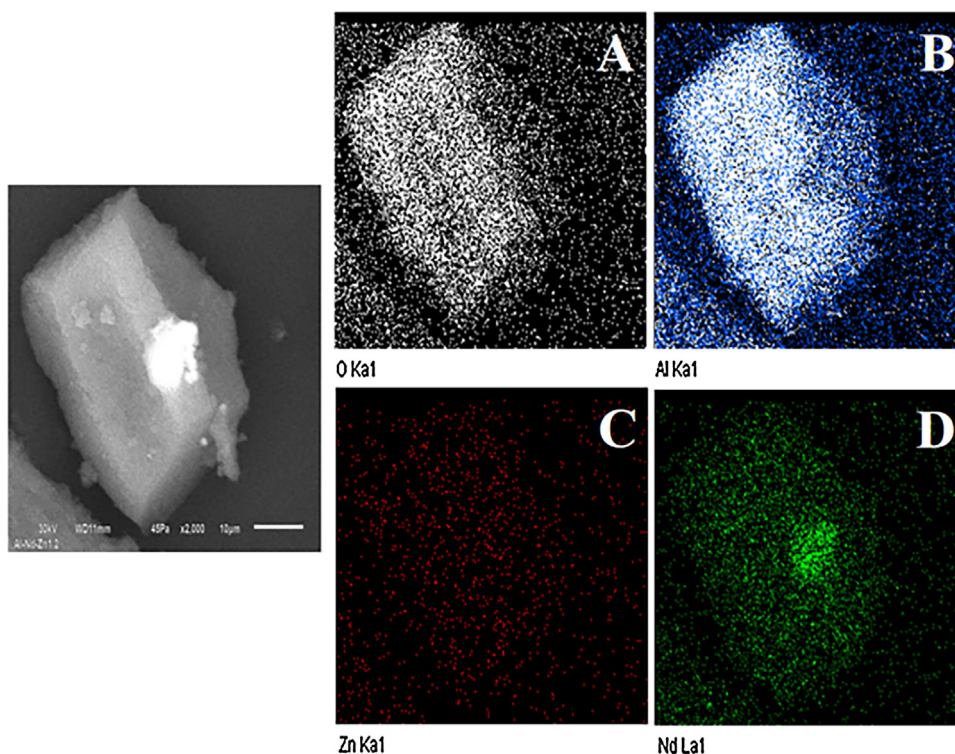

Fig. 3. SEM mapping by element images of the Al-Nd-Zn-1.2 sample: A: Oxygen; B: Aluminum; C: Zinc; D: Neodymium.

(JCPDS card: 10-0425). Whereas, inset in Fig. 1 shows the XRD patterns of pure Nd_2O_3 and ZnO both with an hexagonal structure (JCPDS cards: 75-2255 and 36-1455). XRD patterns of Al-Nd and Al-Nd-Zn-x composite oxides also exhibit diffraction peaks corresponding to the γ-Al_2O_3 phase. However, the intensity of the diffraction peaks of γ-Al_2O_3 decreases with the addition of Nd_2O_3 and ZnO in the Al-Nd-Zn-x composite oxides indicating a decrease in the crystallinity of the γ-Al_2O_3. Furthermore, not any diffraction peak corresponding to the ZnO and Nd_2O_3 phases were observed in either Al-Nd or Al-Nd-Zn-x suggesting that small ZnO and Nd_2O_3

nanoparticles are highly dispersed on the surface and within the γ-Al_2O_3 bulk which are no detected by XRD. The high dispersion of ZnO and Nd_2O_3 nanoparticles in Al-Nd-Zn-x composite oxides is corroborated by TEM (Fig. 2A–D). TEM images of Al-Nd-Zn-1.2 (Fig. 2A and B) and Al-Nd-Zn-2 composite oxides (Fig. 2C and D) exhibit a high dispersion of amorphous nanoparticles of either ZnO or Nd_2O_3 among the γ-Al_2O_3 agglomerates. A homogeneous distribution of O, Zn, Nd and Al species is also corroborated by SEM mapping by element images of the Al-Nd-Zn-1.2 sample (Fig. 3A and D) showing that O, Zn, Nd and Al elements are homogeneously
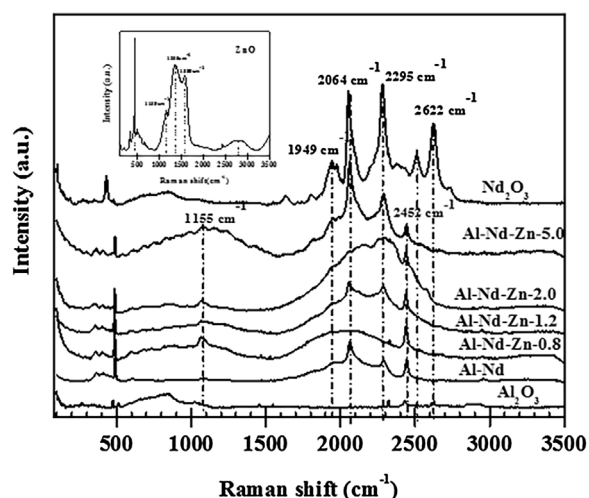
Fig. 4. Raman spectra of γ-Al_2O_3, Al-Nd-Zn-*x* and Nd_2O_3. Inset: Raman spectra of pristine ZnO.

Fig. 6. UV–vis spectra of γ-Al_2O_3, Al-Nd-Zn-*x*, Nd_2O_3 and ZnO.

well dispersed throughout the material. The left image of Fig. 3 shows a big crystal of Al-Nd-Zn-1.2 composite oxide with a tetragonal shape and a white spot on the top surface of the crystal. The big crystal is also observed in the mapping by element images of O (Fig. 3A), Al (Fig. 3B), and Nd (Fig. 3D). While these elements are highly dispersed throughout the Al-Nd-Zn-1.2 material, however, the mapping image of Nd shows a bright and intense green spot on the top of the crystal suggesting the segregation of Nd_2O_3 on the surface of Al-Nd-Zn1.2 composite oxide crystal. On the other hand, in spite that Nd_2O_3 is no detected by XRD however its presence in the Al-Nd-Zn-*x* composite oxides is confirmed by Raman spectroscopy. As shown in Fig. 4, well defined Raman shift bands appear in the Raman spectra of Al-Nd, Al-Nd-Zn-1.2 and Al-Nd-Zn-5 composite oxides at 2064, 2295 and 2452 cm^{-1}. Whereas, the Raman spectra of pure Nd_2O_3 shows Raman shift bands at 440, 1949, 2064, 2295, 2515 and 2622 cm^{-1} which are assigned to the Fg mode and Ag + Eg combination modes of Nd_2O_3 [43–46]. The comparison of the Raman shift bands of Al-Nd and Al-Nd-Zn-*x* composite oxides with those of the Raman spectra of pure Nd_2O_3 it is inferred that these Raman shift bands correspond to electronic transitions between $^4I_{9/2}$ and $^4I_{11/2}$ of Nd^{3+} ions [47]. The intensity of the characteristics vibrational modes of Nd^{3+} transitions in the Al-Nd-Zn-*x* composite oxides increases with the concentration of ZnO as shown in the Al-Nd-Zn-5 composite. This observation suggests that Nd_2O_3 segregation from the Al_2O_3 phase occurred in the
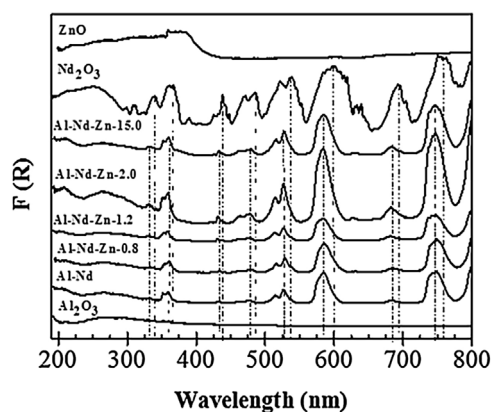
Al-Nd-Zn-*x* composites corroborating the inferred by SEM mapping by element. This is also inferred by Raman microscopy images of Al-Nd-Zn-1.2 and Al-Nd-Zn-2 samples (Fig. 5A and B) showing a segregation of a layer of aggregated Nd_2O_3 particles of blue color on the surface of Al-Nd-Zn-*x* agglomerates. In spite that Raman shift peaks are not well resolved in Al-Nd-Zn-0.8 and Al-Nd-Zn-2 composites, however a broad Raman shift band is observed in the range of 1600–2650 cm^{-1}. It is worth to point out that Raman shift bands of Al-Nd-Zn-*x* composite oxides are broader and less intense than those of pure Nd_2O_3 and are slightly shifted to lower wavenumber which can be attributed to decrease in the particle size of Nd_2O_3 as well as to the chemical interaction between Nd_2O_3 and ZnO species [45,48].

3.3. Optical properties of Al_2O_3-Nd_2O_3-ZnO composite oxides

Diffuse reflectance absorption spectra of γ-Al_2O_3, Nd_2O_3, ZnO, Al_2O_3-Nd_2O_3 and Al-Nd-Zn composite oxides are shown in Fig. 6. UV–vis spectrum of γ-Al_2O_3 shows a broad absorption band of low intensity in the UV region with an absorption edge at about 290 nm that is attributed to charge transfer or the presence of a high density of defects in the structure of γ-Al_2O_3 [49]. Whereas, the UV–vis spectrum of Nd_2O_3 exhibits also a broad absorption band in the UV region with an absorption edge at about 270 nm which is attributed to electronic transitions between the valence band and conduction band of Nd_2O_3 [45,50]. In addition, UV–vis spectrum of Nd_2O_3 shows absorption bands in the UV near and visible region at wavelengths of 339.5, 365.3, 438.3, 485.6, 538.5, 599.0, 693.1 and 758.9 nm that correspond to electronic transitions
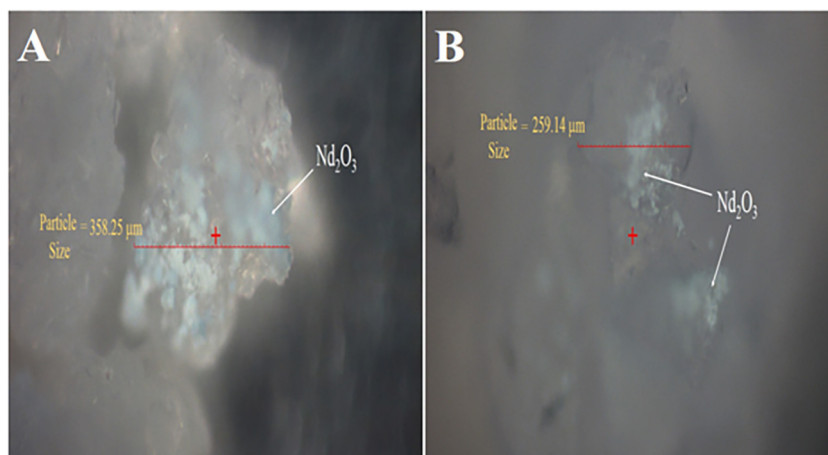

Fig. 5. Raman microscopy images of Al-Nd-Zn-1.2 (A) and Al-Nd-Zn-2 (B).
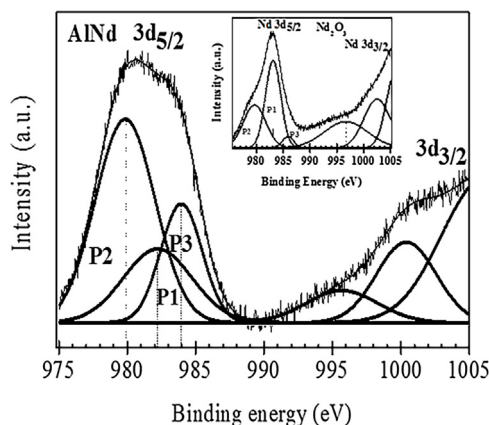
Fig. 7. XPS Nd 3d spectra of Al-Nd composite oxide; Inset: XPS Nd 3d spectra of Nd$_2$O$_3$.

Fig. 8. XPS Nd 3d$_{5/2}$ spectra of Al-Nd-Zn-1.2 composite.

of "4f" orbital of Nd^{3+} in Nd$_2$O$_3$ from the ^{4}I$_{9/2}$ level (4f^3) to higher energy levels [25,51]. Similar to γ-Al$_2$O$_3$ and Nd$_2$O$_3$, UV–vis spectra of Al-Nd and Al-Nd-Zn composite oxides also show a broad absorption band in the UV region with an absorption edge at about 270–290 nm. Furthermore, other narrow and well defined absorption bands are also observed in the UV near and visible region at wavelengths of 332.3, 361.0, 434.0, 478.3, 527.0, 584.4, 684.5 and 747.6 nm that correspond to electronic transitions of "4f" orbital of Nd^{3+} in Nd$_2$O$_3$ [42,43], however, these absorption bands are shifted to lower wavelengths for about 7–15 nm with respect to those of Nd$_2$O$_3$ suggesting that Nd$_2$O$_3$ species are strongly interacting with γ-Al$_2$O$_3$ and ZnO phases. Whereas, ZnO shows a wide absorption band in the wavelengths range from the UV region at 200 nm to the violet-blue at about 430 nm.

The broad absorption band in the UV region with an absorption edge at about 270 − 290 nm in the UV–vis spectra of Nd$_2$O$_3$, Al-Nd and Al-Nd-Zn-*x* composite oxides was chosen for the calculation of their band gap energies due to that this absorption band is attributed to electronic transitions between the valence and conduction bands of Nd$_2$O$_3$ [45,50]. This absorption band was also chosen for the calculation of the band gap energy of γ-Al$_2$O$_3$ because its absorption band is found in the same wavelength range as that of Nd$_2$O$_3$. The band gap energy (E$_g$) values of γ-Al$_2$O$_3$, Nd$_2$O$_3$ and Al-Nd-Zn-*x* composite oxides are shown in Table S1. The calculated E$_g$ for γ-Al$_2$O$_3$ has a value of 3.36 eV. This E$_g$ value is considerably lower than that reported for insulators materials which is typically above 5.0 eV [23,52]. After coupling 15 wt% of Nd$_2$O$_3$ to γ-Al$_2$O$_3$, the E$_g$ value of Al-Nd composite oxide decreased to 3.23 eV being close to that of TiO$_2$ (E$_g$ = 3.2 eV) [53]. Furthermore, with the coupling of ZnO to Al-Nd, the E$_g$ values of Al-Nd-Zn-*x* composite oxides decreased to a minimum value (Eg = 3.08 eV) observed in Al-Nd-Zn-1.2. At higher ZnO content, the E$_g$ values slightly increased in the sequence of 3.1, 3.11 and 3.16 eV for 2.0, 5.0 and 15.0 wt% of ZnO respectively. These Eg values were slightly lower than that reported for the n-type ZnO semiconductor (E$_g$ = 3.2 eV) [35] or the TiO$_2$ semiconductor (E$_g$ = 3.2 eV) [53], whereas the Eg value of pure Nd$_2$O$_3$ was 4.31 eV.

3.4. Chemical state of surface Nd, Al and Zn species

In order to gain an insight of the chemical state of surface Nd, Al and Zn species present in Al-Nd-Zn-*x* composite oxides, XP spectra of Nd$_2$O$_3$, Al-Nd and Al-Nd-Zn-1.2 composite oxides were measured. Inset in Fig. 7 shows high resolution XP spectrum of the Nd 3d transition of Nd$_2$O$_3$. The XP spectrum exhibits two doublets at 983.1 and 1006.6 eV corresponding to 3d$_{5/2}$ and 3d$_{3/2}$ transitions with an energy difference between them of 22.5 eV which is characteristic
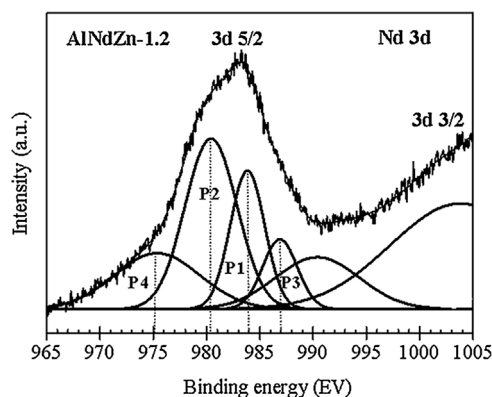
of Nd^{3+}. The Nd 3d$_{5/2}$ transition was fitted in three peaks located at 983.1 (P1), 979.6 (P2) and 985.9 eV (P3). The more intense peak (P1) is ascribed to Nd$_2$O$_3$ [54–56]. Whereas, the appearance of a satellite peak (P2) on the lower energy side at 979.6 eV is attributed to electron transfer from the oxygen ligand to Nd 4f^3 orbital [57,58]. A third peak of lower intensity at 985.9 eV is ascribed to Nd(OH)$_3$ [59]. Fig. 7 shows high resolution XP spectrum of Al-Nd composite oxide. The Nd 3d$_{5/2}$ is fitted also by three peaks located at 979.8 (P2), 982.2 (P1) and 984.0 eV (P3). The intensity of P2 increases significantly in the XP spectrum of Al-Nd with a peak area ratio (A$_{P2}$/A$_{P1}$ = 2.4) higher than that of Nd$_2$O$_3$ (A$_{P2}$/A$_{P1}$ = 0.72). The binding energy value of P2 (E$_b$ = 979.8 eV) is lower than that reported for metallic Nd [54] and it is close to that attributed to 4f^4 orbitals [55]. This observation suggests that there is an increase in the electron transfer to the Nd 4f^3 orbital of Nd$_2$O$_3$ in the Al-Nd composite due to the coupling of γ-Al$_2$O$_3$ and Nd$_2$O$_3$ by the sol-gel method. Whereas, P3 located at 984.0 eV is assigned to Nd(OH)$_3$ [59]. The XP spectrum of Nd 3d$_{5/2}$ transition of Al-Nd-Zn-1.2 composite (Fig. 8) is also fitted by three peaks located at 983.4 (P1), 980.4 (P2) and 986.8 eV (P3) that are assigned to Nd$_2$O$_3$, electron transfer from the oxygen ligand to Nd 4f^3 orbital, and Nd(OH)$_3$ respectively. In addition, a fourth small peak appears at 975.4 eV which is attributed to the coupling signals of 5p^{1}4f^N and the valence band [59]. It is worth to point out that the peak area ratio (A$_{P2}$/A$_{P1}$ = 1.7) of Al-Nd-Zn-1.2 is lower than that of Al-Nd (A$_{P2}$/A$_{P1}$ = 2.4) but higher than that of Nd$_2$O$_3$ (A$_{P2}$/A$_{P1}$ = 0.72). This observation suggests that it might occur electronic transfer from either γ-Al$_2$O$_3$ to ZnO or from γ-Al$_2$O$_3$ to ZnO through Nd$_2$O$_3$. On the other hand, Fig. S2 shows the Al 2p XPS spectrum of Al-Nd-Zn-1.2, whereas inset in Fig. S2 shows the Al 2p XP spectrum of Al$_2$O$_3$. The Al 2p XP spectrum of Al$_2$O$_3$ is fitted in two main peaks located at 74.9 and 77.5 eV and a small peak at 76.0 eV, whereas the spectrum of Al-Nd-Zn-1.2 is fitted in two peaks at 75.1 and 77.8 eV. The peaks at 74.9 and 75.1 eV are ascribed to γ-Al$_2$O$_3$ [60], whereas the peaks at 77.5 and 77.8 eV are attributed to γ-Al$_2$O$_3$ interacting with residual carbon which is arisen from the hexylene glycol used during the synthesis of materials [61] and the small peak at about 76.0 eV is assigned to Al(OH)$_3$ [62]. On the other hand, the XP Zn 2p spectrum of the Al-Nd-Zn-1.2 composite (Fig. S3) exhibit two peaks centered at 1022.6 and 1045.7 eV with an energy spin-orbit splitting between them of 23.1 eV. These E$_b$ values confirms that these peaks correspond to Zn 2p$_{3/2}$ and Zn 2p$_{1/2}$ transitions of Zn^{2+} respectively [63,64].

3.5. Photodegradation of phenol in aqueous medium over Al$_2$O$_3$-Nd$_2$O$_3$-ZnO composite oxides

Earlier studies concerning the photo-catalytic efficiency of Al-Nd-Zn-*x* composite oxides in the photo-degradation of phenol
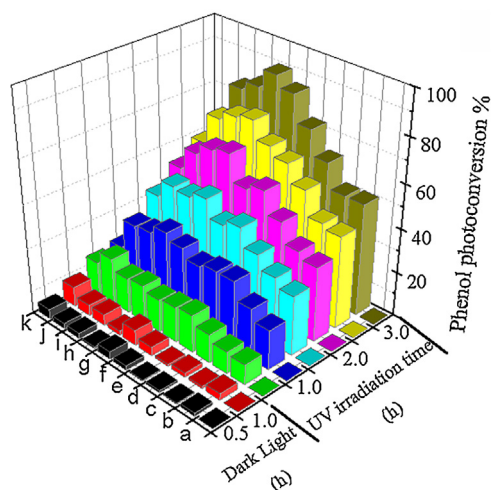
Fig. 9. Phenol adsorption% and phenol photo-conversion% using: a) ZnO; b) TiO$_2$-P25; c) Al$_2$O$_3$ Catapal B; d) γ-Al$_2$O$_3$; e) Al-Nd; f) Al-Nd-Zn-0.8; g) Al-Nd-Zn-1.2; h) Al-Nd-Zn-2.0; i) Al-Nd-Zn-5.0; j) Al-Nd-15.0; and k) Nd$_2$O$_3$.

showed that phenol molecules in aqueous medium (at 80 ppm) were not photo-degraded by UV electromagnetic radiation alone without using the Al-Nd-Zn-*x* photocatalyst (Fig. S4). In order to know about the adsorption capacity of the materials before irradiation with UV light, all solutions where kept under continuous stirring without UV irradiation (dark light) during 1 h. As evidenced, the change in the adsorbed percentage of phenol is scarce without UV irradiation (less than 8.0%) (Fig. 9), indicating that the adsorption phenomena is not occurring significantly before irradiation starts. The percentage of photo-converted phenol using γ-Al$_2$O$_3$ and Al-Nd-Zn-*x* composite materials prepared by the sol-gel method and pristine ZnO, Al$_2$O$_3$ Catapal B, TiO$_2$-P25, and Nd$_2$O$_3$ as reference photocatalysts is shown in Fig. 9. The photo-degradation of phenol (80 ppm) using Al$_2$O$_3$-Catapal B and TiO$_2$-P25 (Degussa) as reference photocatalysts showed a photo-conversion of aqueous phenol of about 50% after 3 h of UV irradiation time (Fig. 9).Whereas, pristine ZnO did not show any photo-conversion of phenol after 3 h of UV light irradiation. However, it was observed an improvement in the photo-conversion of phenol in the γ-Al$_2$O$_3$ prepared by the sol-gel method showing a phenol photo-conversion of about 60% after 3 h of UV irradiation (Fig. 9). When 15 wt% of Nd$_2$O$_3$ was coupled to the γ-Al$_2$O$_3$ by the sol-gel method (Al-Nd composite) an improvement in the phenol photo-conversion was observed increasing to approximately 72.0% after 3 h of UV irradiation (Fig. 9). Furthermore, when 0.8 wt% of ZnO was coupled to the Al-Nd composite by the sol-gel method, the phenol photo-conversion using the Al-Nd-Zn-0.8 composite was improved to 85.0% after 3 h of UV irradiation. The photo-conversion of phenol was enhanced to a maximum by increasing the concentration of ZnO in the composite to 1.2 wt% (Al-Nd-Zn-1.2) reaching 90.0% of photo-converted phenol after only 3 h of UV irradiation (Fig. 9). The photo-conversion of aqueous phenol using the Al-Nd-Zn-1.2 composite was improved for approximately 25.0% with respect to that of Al-Nd composite when 1.2% of ZnO was coupled by the sol-gel method. This result also shows that the phenol photo-conversion using the Al-Nd-Zn-1.2 composite is nearly 1.5 times that exhibited by the γ-Al$_2$O$_3$ prepared by the sol-gel method of the present work and approximately 1.8 times that shown by the commercial Al$_2$O$_3$-Catapal B and TiO$_2$-P25 respectively. By increasing the concentration of ZnO in the Al-Nd-Zn composites to 2.0 and 5.0 wt%, the photo-conversion of phenol was also high but less than that of Al-Nd-Zn-1.2 photocatalyst, photo-converting about 82.0% and 78.0% respectively after 3 h of UV irradiation (Fig. 9). At higher ZnO concentration, the photo-conversion of phenol decreased as in
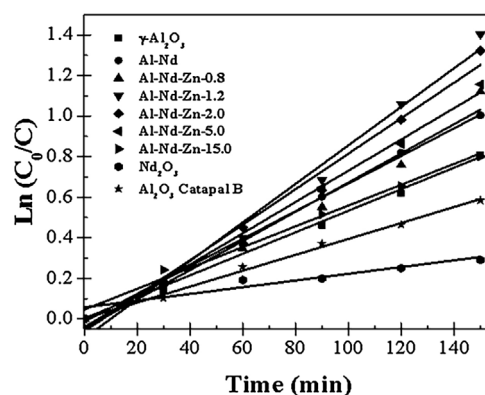

Fig. 10. Ln(C$_0$/C) vs. Reaction time in the degradation of phenol using Al-Nd-Zn composite oxides prepared by sol-gel. For comparison, reaction kinetics of γ-Al$_2$O$_3$, Nd$_2$O$_3$, Al$_2$O$_3$ Catapal B and TiO$_2$-P25 are also shown.

Table 2
Rate constant (k) and half life time (t$_{1/2}$) in the photodegradation of phenol using Al-Nd-Zn as photocatalysts and 3 h of UV irradiation. For comparison, k and t$_{1/2}$ for Al$_2$O$_3$ Catapal-B and TiO$_2$-P25 are also shown.

Photocatalyst	k × 10^{-3}(min^{-1})	t$_{1/2}$(min)
γ-Al$_2$O$_3$	5.0	138.0
Al-Nd	8.0	87.0
Al-Nd-Zn-0.8	9.0	77.0
Al-Nd-Zn-1.2	12.0	58.0
Al-Nd-Zn-2.0	9.0	77.0
Al-Nd-Zn-5.0	8.0	87.0
Al-Nd-Zn-15.0	4.0	173.0
Nd$_2$O$_3$	1.0	693.0
Al$_2$O$_3$ Catapal B	3.0	231.0
TiO$_2$-P25	3.0	231.0

the case of the Al-Nd-Zn-15.0 composite photo-converting about 61.0% after 3 h of UV irradiation. On the other hand, the photo-conversion of phenol using pure Nd$_2$O$_3$ as reference photocatalyst that was prepared by decomposition of neodymium acetylacetonate at 800 °C by 4 h was only of 28.0% after 3 h of UV irradiation. The kinetics data in the photodegradation of phenol using Al-Nd-Zn-*x* composite oxides were fitted to a pseudo first-order equation using the Langmuir-Hinshelwood model that has been often used to describe the kinetics of photocatalytic reactions of organic compounds in aqueous solutions [65,66]:

$$Ln(C_0/C) = kt \qquad (2)$$

The Ln (C$_0$/C) versus reaction time (t) plots are linear indicating that photo-degradation kinetics adjusts well to a pseudo first-order equation (Fig. 10). The reaction rate constant (k) calculated by linearization of the curves and the half-life time (t$_{1/2}$) are shown in Table 2. Al-Nd mixed oxide exhibited an improved kinetic behavior (k = 8.0 × 10^{-3} min^{-1} and t$_{1/2}$ = 87.0 min) comparatively with that of γ-Al$_2$O$_3$ (k = 5.0 × 10^{-3} min^{-1} and t$_{1/2}$ = 138.0 min). Furthermore, an enhancement in the efficiency for the elimination of phenol in aqueous medium was observed when ZnO is added to Al-Nd mixed oxide by the sol-gel method as shown by an increase in the reaction rate constant and a decrease in the half life time (Table 2). Al-Nd-Zn-1.2 was the photocatalyst with the highest efficiency for the elimination of phenol in aqueous medium as shown by its highest reaction rate constant (k = 12.0 × 10^{-3} min^{-1}) and its lower half life time (t$_{1/2}$ = 58.0 min) in the photocatalysts series. However, when the ZnO concentration in the ternary oxide was 15.0 wt%, the Al-Nd-Zn-15.0 photocatalyst showed a kinetic behavior similar to the one corresponding to the γ-Al$_2$O$_3$ characterized by a low reaction rate constant and a high half-life time. For comparison, Al$_2$O$_3$ Catapal B, TiO$_2$-P25 and Nd$_2$O$_3$ prepared by decomposition of acetylacetonate
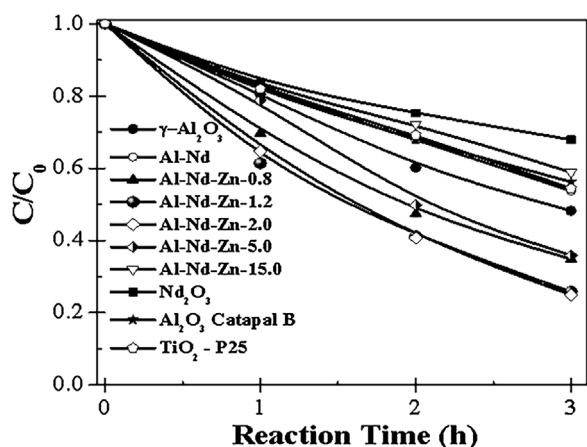
Fig. 11. Total organic carbon (TOC) of the phenol dissolution versus irradiation time using Al-Nd-Zn-*x* photocatalysts.

showed the lowest efficiency for the elimination of phenol in aqueous medium as corroborated by their lowest reaction rate constant and highest half-life time in the photocatalyst series (Table 2).

To learn about the influence of the sample weight on the reaction kinetics in the photo-degradation of phenol in aqueous medium, γ-Al$_2$O$_3$ and Al-Nd-Zn-2.0 composite oxide were tested by using various sample weights in the range of 0.25–1.5 g/L of aqueous phenol. Fig. S5 shows the reaction rate constant as a function of the weight of photo-catalyst per volume of aqueous phenol. It is observed an increase in the reaction rate constant with the increase in the sample weight of the photocatalyst after 3 h of UV irradiation and there is no significant increase in the reaction rate constant at contents higher than 1 mg of sample per 1 mL of aqueous phenol, indicating that this ratio (1:1) is the optimal one in order to obtain the highest efficiency in the photo-conversion of phenol in aqueous medium, when the concentration of phenol is 80 ppm. In our case we use 1.0 g/L of solid for the photoactivity test which is nearly the limit where the maximum efficiency of the Al-Nd-Zn-*x* photocatalysts in the photodegradation of phenol is reached. The total organic carbon analysis (TOC) of irradiated solutions is shown in Fig. 11. It is observed a higher decrease in the relative concentration (C/C$_0$) of organic carbon in the Al-Nd-Zn photocatalysts with 0.8, 1.2, and 2.0 wt% of ZnO compared with those of Al-Nd-Zn-5.0, γ-Al$_2$O$_3$, Al-Nd, Al$_2$O$_3$-Catapal B, TiO$_2$-P25, Al-Nd-Zn-15.0 and Nd$_2$O$_3$ indicating a high mineralization of dissolved organic carbon to CO$_2$ after 3 h of UV irradiation. The mineralization of organic carbon using Al-Nd-Zn-0.8 as photocatalyst was about 65%, whereas Al-Nd-Zn-1.2 and Al-Nd-Zn-2.0 mineralize about 75.0%. The identification of residual intermediates was carried by calculation of the concentration of the possible intermediaries, 1,4-benzoquinone and hydroquinone, at the wavelengths 245 and 283 nm respectively. Fig. S6-A shows the UV–vis spectra of phenol after UV light irradiation during 6 h using Al-Nd-Zn-1.2 and Fig. S6-B shows the UV–vis spectra of the possible intermediaries (1,4-benzoquinone and hydroquinone) and phenol. By comparing both UV–vis spectra it is concluded that the formation of 1,4-benzoquinone and hydroquinone is scarce due to that almost all the dissolved organic carbon was mineralized to CO$_2$. When the fotodegradation of phenol was carried out in a period of 60 min, it was possible detect the formation of a minimum concentration of 1,4-benzoquinone and hydroquinone. Fig. S7 shows the UV–vis spectra of phenol solution after UV light irradiation for a period of 60 min using γ-Al$_2$O$_3$ and Table S2 shows the calculated concentration of 1,4-benzoquinone, hydroquinone and phenol as a function of the UV light irradiation time. It can be observed that the concentration of phenol decreases with the photoreaction time from 0.000924 molL^{-1} to

0.000686 molL^{-1} during a period of 60 min. Whereas a low concentration of 1,4-benzoquinone (0.0000337 molL^{-1}) appears after 5 min of photoreaction and increases to 0.000318 molL^{-1} after 60 min of photoreaction. On the other hand, a too much low concentration of hydroquinone (0.000000234 molL^{-1}) is seen only after 30 min of photoreaction and increases to 0.00000598 molL^{-1} after 60 min of photoreaction. On the other hand, when Al-Nd-Zn-1.2 is used as photocatalyst (Fig. S8, Table S3), the concentration of phenol decreases with the UV light irradiation time from 0.00092 molL^{-1} to 0.00064 molL^{-1} during 60 min of photoreaction. In contrast to the relatively short reaction time needed for the appearance of 1,4-benzoquinone over γ-Al$_2$O$_3$, the appearance of this intermediary over Al-Nd-Zn-1.2 occurred after 15 min of photoreaction with a concentration of 0.0000519 molL^{-1} and increased with the reaction time to reach 0.000294 molL^{-1} during 60 min of photoreaction. Furthermore, the formation of hydroquinone is not observed over Al-Nd-Zn-1.2 in the first 60 min of photoreaction. This observation suggests that the formation of 1,4-benzoquinone and hydroquinone is inhibited when Al-Nd-Zn-1.2 is used as photocatalyst. In this sense, γ-Al$_2$O$_3$ favors the formation of intermediaries more quickly in the first 60 min of reaction, while the conversion of phenol is more slow. In contrast, when Al-Nd-Zn-1.2 is used as photocatalyst, the formation of intermediaries is retarded in the first 60 min of reaction and the conversion of phenol is more rapid than that of γ-Al$_2$O$_3$. This observation corroborates the high efficacy of the Al-Nd-Zn-1.2 photocatalyst to photodegradate phenol and mineralize dissolved organic carbon to CO$_2$.

3.6. Photocatalytic performance of Al$_2$O$_3$-Nd$_2$O$_3$-ZnO composite oxides

The high photocatalytic activity in the degradation of phenol exhibited by the γ-Al$_2$O$_3$ prepared by the sol gel method can be explained by its low band gap energy (E$_g$ = 3.36 eV) being close to that shown by a semiconductor material. Concerning to it, it is known that the decrease of the band gap energy of γ-Al$_2$O$_3$ induces a shift in the position of the Fermi level that can be correlated with the ability of the γ-Al$_2$O$_3$ surface to give or accept electrons [67,68]. The Fermi level is modified by the presence of defects or vacancies in the structure of γ-Al$_2$O$_3$ [22]. It has been also shown that a decrease of the Fermi level gives rise to an increase in the donor behavior of the γ-Al$_2$O$_3$ surface and thereby the decrease in its band gap energy can cause the modification in its surface chemistry [67,69]. In the γ-Al$_2$O$_3$ prepared by the sol-gel method there is a decrease in its band gap energy implying that there is an increase in the ability of its surface to give electrons (e$^-$) and leaving a high amount of holes (h$^+$) under UV light irradiation. This is consistent because its absorption band is located in the UV region at about 290 nm which is attributed to the presence of a high density of defects in the structure of γ-Al$_2$O$_3$ [49]. Concerning to it, it is reported that the presence of structural defects in the γ-Al$_2$O$_3$ decreases its band gap energy from 8.7 eV to 2.5 eV at the surface, therefore such a surface cannot be considered as an insulating but as a new phase with properties similar to a semiconductor [67]. This characteristic is correlated to the acid − base properties of the γ-Al$_2$O$_3$ surface [67] which would explain its photocatalytic activity. Therefore, it is suggested that due to the low E$_g$ (3.36 eV) of the γ-Al$_2$O$_3$ prepared by the sol-gel method its surface should supply unpaired electrons (e$^-$) to the conduction band under excitation with UV light, leaving a high amount of holes (h$^+$) sites for the adsorption of OH$^-$ ions to produce OH^0 radicals highly oxidant of phenol molecules in aqueous medium. The degradation of the phenol molecules with UV light irradiation is effectively possible due to that the wavelength of the absorption edge of the γ-Al$_2$O$_3$ (λ = 290 nm) is close to that of the UV light irradiation
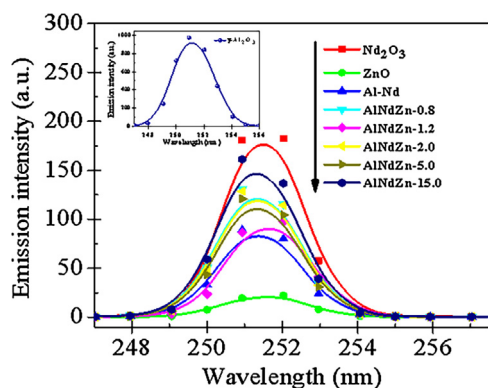
Fig. 12. Fluorescence spectra of γ-Al_2O_3, Nd_2O_3, Al-Nd and Al-Nd-Zn-x composite oxides.

lamp ($\lambda = 254$ nm) and that of phenol molecules ($\lambda = 270$ nm). On the other hand, the trend in photo-degradation kinetics of phenol indicates that photocatalytic activity of γ-Al_2O_3 is improved by coupling 15 wt% of Nd_2O_3 and a concentration less than 2.0 wt% of ZnO by the sol-gel method. The photocatalytic activity of Al-Nd is improved about 20.0% with respect to that of γ-Al_2O_3. Such improvement is due to that the coupling between γ-Al_2O_3 and Nd_2O_3 favors the electronic transfer from the γ-Al_2O_3 surface to the incomplete Nd $4f^3$ orbitals of Nd_2O_3 as inferred from the XPS studies of Al-Nd. Such coupling of γ-Al_2O_3 with Nd_2O_3 might forms a space-charge region in the interface between both phases and act as an electron trap for the separation of charges and thereby to decrease the recombination rate of photogenerated electron-hole pairs. The decrease in the recombination rate of electron–hole pair of γ-Al_2O_3 was investigated with fluorescence spectroscopy. Fig. 12 shows the emission spectra of γ-Al_2O_3, Nd_2O_3, Al-Nd and Al-Nd-Zn-x after excitation with a wavelength of 250 nm. The intensity of emission spectra of Al-Nd composite oxide decreases significantly with respect to that of γ-Al_2O_3 (Inset in Fig. 12) and Nd_2O_3 implying that the recombination rate of electron–hole pairs is effectively decreased. Therefore, such decrease in the intensity of the fluorescence spectra of Al-Nd confirms that Nd_2O_3 acts as an electron trap for the separation of photoinduced charges favoring the improvement in the photocatalytic activity. On the other hand, when ZnO is coupled to Al-Nd, the intensity of the emission spectra of Al-Nd-Zn-1.2 decreased to a level comparable to that observed in Al-Nd. At higher ZnO content, the intensity of their fluorescence spectra was higher than that observed in Al-Nd and Al-Nd-Zn-1.2 composite oxides but lower than those of γ-Al_2O_3 and Nd_2O_3. This suggests that the decrease in the recombination rate depends strongly on the composition of the material, specifically on the concentration of ZnO in the Al-Nd-Zn-x composite oxides. The lower intensity of the emission spectra of Al-Nd-Zn-1.2 indicates that the recombination rate of photogenerated charge carrier was inhibited greatly in this composite oxide. Furthermore, this material exhibited the lower E_g (3.08 eV) which can be correlated with a higher ability of the γ-Al_2O_3 surface to donate electrons (e^-) and leaving holes (h^+). This corroborates that Al-Nd-Zn-1.2 is the highest efficient photocatalytic material to photoconvert phenol molecules. On the other hand, the fluorescence spectra of ZnO shows the lowest intensity indicating that the recombination rate of electron-hole pairs is highly restrained in this material. However, ZnO was no active in the photo-conversion of phenol which can be explained because to that phenol is a very stable molecule which is difficult of degrading. Although, ZnO has an E_g of 3.2 eV indicating that it might be active with UV light, however it is an n-type semiconductor which contains a higher concentration of electrons (e^-) than holes (h^+). Concerning to it, it is known that the h^+ sites are essential for the

oxidation of phenol molecules, therefore the inactivity of ZnO is due to the scarcity of h^+ sites in addition to its high crystallinity and low S_{BET} (6.0 m^2/g). Therefore, the role of coupling ZnO to the Al-Nd composite oxide is also as an electron trap for the separation of photogenerated charges. This is consistent because the intensity of the peak at 980.42 eV in the XPS $3d_{5/2}$ spectrum of Al-Nd-Zn-1.2 which is attributed to electron transfer from the valence band to the Nd $4f^3$ orbital decreases with respect to that of Al-Nd which can be explained because γ-Al_2O_3 may donate electrons to the conduction band of the n-type ZnO semiconductor. Therefore ZnO may acts also as an electron trap for separation of charges and thereby to decrease the recombination rate of electron-hole pairs. The same argument can explain the high photocatalytic activity observed in Al-Nd-Zn-x composites with ZnO concentration in the range 0.8–2.0 wt%. It is worth to point out that these materials are highly active to photodegradate phenol only under UV light irradiation due to that phenol molecules cannot be oxidized with the generation of holes (h^+) using visible light [70] since the absorption band responsible to photodegradate phenol molecules is situated only in the UV region, therefore these materials not shown photocatalytic activity in the degradation of phenol with visible or sun light (Fig. S9). These materials showed high efficiency to photo-convert phenol at high concentration of contaminant (80 ppm) and mineralize dissolved organic carbon to CO_2 under UV light. The preparation of Al-Nd-Zn-x composites by the sol-gel method contributes to obtain homogeneous materials with high specific surface area which could be beneficial to obtain a high amount of active sites and thereby for the photoconversion of phenol in aqueous medium. On the other hand, the generation of Al-Nd-Zn-x composites with bimodal pore size distributions could be suitable to ease the diffusion of phenol molecules to the active sites. Whether charge carrier transfer or the specific surface area and pore size distributions of the Al-Nd-Zn-x composites have a stronger influence on their efficacies in the photodegradation of phenol in aqueous medium, however these properties are not separated and both of them contribute to the improvement in the photocatalytic activity.

4. Conclusions

Coupled Al-Nd-Zn-x composite oxides were prepared by the sol-gel method and tested in the photocatalytic degradation of phenol in aqueous medium. Al-Nd-Zn-x composites with ZnO concentration in the range 0.8–2.0 wt% showed high efficiency to photo-convert phenol and mineralize dissolved organic carbon to CO_2. The Al-Nd-Zn-1.2 composite was the material with the highest efficacy to photodegradate phenol in aqueous medium photo-converting about 90% of phenol and mineralizing 75.0% of dissolved organic carbon to CO_2 after only 3 h of UV irradiation. It is proposed that the intimate contact between γ-Al_2O_3, Nd_2O_3 and ZnO phases are beneficial characteristics for the separation of the photogenerated charge carriers in order to prevent the recombination rate of photogenerated electron-hole pairs. These materials have high BET specific surface areas and bimodal pore size distributions which are excellent characteristics for the adsorption and diffusion of phenol molecules to the active sites resulting in an enhanced photocatalytic activity for the degradation of phenol in aqueous medium using UV light.

Appendix A. Supplementary data

Supplementary data associated with this article can be found, in the online version, at http://dx.doi.org/10.1016/j.apcatb.2017.02.030.

References

[1] M.T. Pinho, H.T. Gomes, R.S. Ribeiro, J.L. Faria, A.M. Silva, Appl. Catal. B Environ. 165 (2015) 706–714.
[2] E. Saputra, S. Muhammad, H. Sun, H.M. Ang, M.O. Tadé, S. Wang, Appl. Catal. B Environ. 142–143 (2013) 729–735.
[3] G. Colon, J.M. Sanchez-España, M.C. Hidalgo, J.A. Navio, J. Photochem. Photobiol. A: Chem. 179 (2006) 20–27.
[4] H.R. Mortaheb, M.H. Amini, F. Sadeghian, B. Mokhtarani, H. Daneshyar, J. Hazard. Mater. 160 (2008) 582–588.
[5] D. Mantzavinos, E. Psillaski, J. Chem. Technol. Biotechnol. 79 (2004) 431–454.
[6] M.A. Estévez, E.L. Peragio, E.M. Carballo, J.S. Gándara, J.C. Mejunto, L.G. Río, Agric. Acosyst. Environ. 123 (2008) 247–260.
[7] A. Al-Kdasi, A. Idris, K. Saed, Glob. Nest: Int. J. 6 (2004) 222–230.
[8] N. Daneshvar, D. Salari, A. Niaei, A.R. Khataee, J. Environ. Sci. Health B 41 (2006) 1273–1290.
[9] G. Liu, X. Li, J. Zhao, Environ. Sci. Tecnol. 34 (2000) 3982–3990.
[10] M.F. Almeida, C.R. Bellato, A.H. Mounteer, S.O. Ferreira, J.L. Milagres, L.D.L. Miranda, Appl. Surf. Sci. 357 (2015) 1765–1775.
[11] J.J. Murcia, M.C. Hidalgo, J.A. Navío, J. Araña, J.M. Doña-Rodriguez, Appl. Catal. B Environ. 179 (2015) 305–312.
[12] S.H. Lin, C.H. Chiou, C.K. Chang, R.S. Juang, J. Environ. Manag. 92 (2011) 3098–3104.
[13] R.P. Parra, I.H. Perez, M.E. Rincon, S.L. Ayala, M.C.R. Ahumada, Sol. Energy Mater. Sol. Cells 76 (2003) 189–199.
[14] H. Ma, J. Shen, M. Shi, X. Lu, Z. Li, Y. Long, N. Li, M. Ye, Appl. Catal. B 121–122 (2012) 198–205.
[15] E. Dvininov, M. Ignat, P. Barvinschi, M.A. Smithers, E. Popovici, J. Hazard. Mater. 177 (2010) 150–158.
[16] A. Mantilla, F. Tzompantzi, J.L. Fernández, J.A.I. Díaz Góngora, G. Mendoza, R. Gómez, Catal. Today 150 (2010) 353–357.
[17] G. Mendoza-Damián, F. Tzompantzi, A. Mantilla, A. Barrera, L. Lartundo-Rojas, J. Hazard. Mater. 263 (2013) 67–72.
[18] Y. Guo, D. Li, Ch. Hua, Y. Wang, E. Wang, Y. Zhoub, S. Feng, Appl. Catal. B: Environ. 30 (2001) 337–347.
[19] P.A. Deshpande, G. Madras, Chem. Eng. J. 161 (2010) 136–145.
[20] A. Barrera, F. Tzompantzi, V. Lara, R. Gómez, J. Photochem. Photobiol. A: Chem. 227 (2012) 45–50.
[21] A. Barrera, F. Tzompantzi, J.M. Padilla, J.E. Casillas, G. Jácome-Acatitla, M.E. Cano, R. Gómez, Appl. Catal. B 144 (2014) 362–368.
[22] F. Tzompantzi, Y. Piña, A. Mantilla, O. Aguilar-Martinez, F. Galindo-Hernández, X. Bokhimi, A. Barrera, Catal. Today 220–222 (2014) 49–55.
[23] I. Chorkendorff, J.W. Niemantsverdriet, Concepts of Modern Catalysis and Kinetics, Wiley-VCH GmbH & Co KGaA, Chap. 6 p. 233.
[24] Y. Ozawa, Y. Tochihara, M. Nagai, S. Omi, Catal. Commun. 4 (2003) 87–90.
[25] F. Oudet, P. Courtine, A. Vejux, J. Catal. 114 (1988) 112–120.
[26] U.G. Akpan, B.H. Hameed, Appl. Catal. A. 375 (2010) 1–11.
[27] T.L.R. Hewer, E.C.C. Souza, T.S. Martins, E.N.S. Muccillo, R.S. Freire, J. Mol. Catal. A: Chem. 336 (2011) 58–63.
[28] T. Kawahara, Y. Konishi, H. Tada, N. Tohge, S. Ito, Langmuir 17 (2001) 7442–7445.
[29] J. Shang, W.Q. Yao, Y.F. Zhu, N.Z. Wu, Appl. Catal. A 257 (2004) 25–32.
[30] C.F. Lin, C.H. Wu, Z.N. Onn, J. Hazard. Mater. 154 (2008) 1033–1039.
[31] J. Georgieva, S. Sotiropoulos, S. Armyanov, N. Philippidis, I. Poulios, J. Appl. Electrochem. 4 (2001) 173–181.
[32] E. Rodríguez, G. Fernández, B. Ledesma, P. Álvarez, F.J. Beltrán, Appl. Catal. B: Environ. 92 (2009) 240–249.
[33] O. Vázquez-Cuchillo, A. Cruz-López, L.M. Bautista-Carrillo, A. Bautista-Hernández, L.M. Torres Martínez, S. Wohn Le, Res. Chem. Intermed. 36 (2010) 103–113.
[34] A. Fujishima, T. Rao, D. Tryk, Titanium dioxide photocatalys, J. Photochem. Photobiol. C 1 (2001) 1–21.
[35] R.E. Marotti, P. Giorgi, G. Machado, E.A. Dalchiele, Sol. Energy Mater. Sol. Cells 90 (2006) 2356–2361.
[36] G. Marcì, V. Augugliaro, M. López-Muñoz, C. Martín, L. Palmisano, V. Rives, M. Schiavello, R.J.D. Tilley, A.M. Venezia, J. Phys. Chem. B 105 (2001) 1033–1040.
[37] M. Vaseem, A. Umar, Ahmad, Y.B. Hahn, ZnO Nanoparticles: Growth, Properties, and Applications. Metal Oxide Nanostructures and Their Applications, American Scientific Publ., 2010, pp. 1–36.
[38] J.S. Valente, F. Tzompantzi, J. Prince, J.G.H. Cortez, R. Gomez, Appl. Catal. B Environ. 90 (2009) 330–338.
[39] D.L. Pavia, G.M. Lampman, G.S. Kriz, Introduction to Spectroscopy, 4th ed., Cengage Learning, Bellingham, Washington, 2009.
[40] P. Padhye, P. Poddar, J. Mater. Chem. A 2 (2014) 19189–19200.
[41] S. Lowell, J.E. Shields, M.A. Thomas, in: M. Thommes (Ed.), Characterization of Porous Solids and Powders: Surface Area, Pore Size and Density, Springer Netherlands, 2004, 2017, pp. 31–32.
[42] K.W.S. Sing, D.H. Everet, R.A.W. Haul, L. Moscou, R.A. Pierotti, J. Rouquerol, T. Siemieniewska, Pure Appl. Chem. 57 (1985) 603–619.
[43] R. Yuvakkumar, S.I. Hong, J. Sol-Gel Sci. Technol. 73 (2015) 511–551.
[44] B. Umesh, B. Eraiah, H. Nagabhushana, S.C. Sharma, D.V. Sunitha, B.M. Nagabhushana, C. Shivakumara, J.L. Rao, R.P.S. Chakradhar, Spectrochim. Acta Part A 93 (2012) 228–234.
[45] B. Umesh, B. Eraiah, H. Nagabhushana, B.M. Nagabhushana, G. Nagaraja, C. Shivakumara, R.P.S. Chakradhar, J. Alloys Compd. 509 (2011) 1146–1151.
[46] A. Ubaldini, M.M. Carnasciali, J. Alloys Compd. 454 (2008) 374.
[47] Y. Xu, J. Wu, W. Sun, D. Tao, L. Yang, Z. Song, S. Weng, Z. Xu, R.D. Soloway, D. Xu, G. Xu, Chem. Eur. J. 8 (23) (2002) 5323–5331.
[48] T. Bilajan, S. Roncevic, Z. Meic, K. Kovac, Chem. Phys. Lett. 395 (2004) 246.
[49] G. Pérez, S. Fuentes, V. Petranovskii, A. Simakov, Catal. Lett. 110 (2006) 53–60.
[50] L.K. Pan, Q.S. Chang, C.M. Li, J. Phys. Chem. B 108 (2004) 3404–3406.
[51] P. Caro, Structure Electronique des Elements de Transition, 1st ed., Presses Universitaires de France, Paris, 1976.
[52] B. Shin, J.R. Weber, R.D. Long, P.K. Hurley, C.G. Van de Walle, P.C. Mclntyre1, Appl. Phys. Lett. 96 (15) (2010) 152908.
[53] C. Dette, M. Pérez-Osorio, C.S. Kley, P. Punke, C.E. Patrick, P. Jacobson, F. Giustino, S. Jung, K. kern, Nano Lett. 14 (2014) 6533–6538.
[54] C.J. Powell, Recommended Auger parameters for 42 elemental solids, J. Electron. Spectrosc. Relat. Phenom. 185 (2012) 1–3.
[55] B. Glorieux, R. Berjoan, M. Matecki, A. Kammouni, D. Perarnau, Appl. Surf. Sci. 253 (2007) 3349–3359.
[56] J.F. Moulder, W.G. Stickle, P.E. Sobol, K.D. Bomben, Handbook of X-Ray Photoelectron Spectroscopy, 1995, pp. 62.
[57] F.J. Jing, F.Y. Jin, Y.W. Liu, G.J. Wan, X.M. Liu, X.B. Zhao, R.K.Y. Fu, Y.K. Leng, N. Huang, P.K. Chu, J. Vac. Sci. Technol. A 24 (5) (2006) 1790–1794.
[58] E. Talik, J. Alloys Compd. 377 (2004) 259–267.
[59] D.F. Mullica, C.K.C. Lok, H.O. Perkins, G.A. Benesh, V. Young, J Electron. Spectrosc. Relat. Phenom. 71 (1995) 1–20, D.
[60] T.L. Barr, J. Phys. Chem. 82 (16) (1978) 1801–18010.
[61] C.S. Maldonado, J.R. De la Rosa, C.J. Lucio-Ortíz, A. Hernández-Ramírez, F. Castillón-Barraza, J. Sánchez-Valente, Materials 7 (2014) 2062–2086.
[62] J.R. Lindsay, H.J. Rose, W.E. Swartz, D.H. Watts, K.A. Rayburn, Appl. Spectrosc. 27 (1973) 1.
[63] J. Wang, H. Li, S. Meng, L. Zhang, X. Fu, S. Chen, Appl. Catal. B Environ. 200 (2017) 19–30.
[64] Z. Zhao, J. Song, J. Zheng, J. Lian, Trans. Nonferrous Met. Soc. China 24 (2014) 1434–1439.
[65] A. Sobczynski, Ł. Duczmal, W. Zmudzinski, J. Mol. Catal. A: Chem. 213 (2004) 225–230.
[66] K. Porkodi, K.V. Kumar, Appl. Catal. B 79 (2008) 108–109.
[67] B. Ealet, M.H. Elyakhloufi, E. Gillet, M. Ricci, Thin Solid Films 250 (1994) 92–100.
[68] W.M. Mullins, B.L. Averbach, Surf. Sci. 206 (1988) 52.
[69] W.M. Mullins, Surf. Sci. 217 (1989) 459.
[70] H. Zhu, X. Chen, Z. Zheng, X. Ke, E. Jaatinen, J. Zhao, C. Guo, T. Xie, D. Wang, Chem. Commun. (2009) 7524–7526.